

## MIT Open Access Articles

*Superconducting nanowire single-photon detectors integrated with optical nano-antennae*

The MIT Faculty has made this article openly available. **Please share** how this access benefits you. Your story matters.

**Citation:** Hu, Xiaolong et al. "Superconducting Nanowire Single-photon Detectors Integrated with Optical Nano-antennae." *Optics Express* 19.1 (2010): 17. © 2010 The Optical Society

**As Published:** <http://dx.doi.org/10.1364/OE.19.000017>

**Publisher:** Optical Society of America

**Persistent URL:** <http://hdl.handle.net/1721.1/73446>

**Version:** Final published version: final published article, as it appeared in a journal, conference proceedings, or other formally published context

**Terms of Use:** Article is made available in accordance with the publisher's policy and may be subject to US copyright law. Please refer to the publisher's site for terms of use.



**This paper was published in Optics Express and is made available as an electronic reprint with the permission of OSA. The paper can be found at the following URL on the OSA website:  
<http://www.opticsinfobase.org/abstract.cfm?URI=oe-19-1-17>.  
Systematic or multiple reproduction or distribution to multiple locations via electronic or other means is prohibited and is subject to penalties under law.**

# Superconducting nanowire single-photon detectors integrated with optical nano-antennae

Xiaolong Hu,<sup>1,\*</sup> Eric A. Dauler,<sup>2</sup> Richard J. Molnar,<sup>2</sup>  
and Karl K. Berggren<sup>1,3</sup>

<sup>1</sup>Research Laboratory of Electronics, Massachusetts Institute of Technology,  
77 Massachusetts Avenue, Cambridge, Massachusetts 02139, USA

<sup>2</sup>Lincoln Laboratory, Massachusetts Institute of Technology,  
Lexington, Massachusetts 02420, USA

<sup>3</sup>Berggren@mit.edu

\*XLHu@mit.edu

**Abstract:** Optical nano-antennae have been integrated with semiconductor lasers to intensify light at the nanoscale and photodiodes to enhance photocurrent. In quantum optics, plasmonic metal structures have been used to enhance nonclassical light emission from single quantum dots. Absorption and detection of single photons from free space could also be enhanced by nanometallic antennae, but this has not previously been demonstrated. Here, we use nano-optical transmission effects in a one-dimensional gold structure, combined with optical cavity resonance, to form optical nano-antennae, which are further used to couple single photons from free space into a 80-nm-wide superconducting nanowire. This antenna-assisted coupling enables a superconducting nanowire single-photon detector with 47% device efficiency at the wavelength of 1550 nm and 9- $\mu\text{m}$ -by-9- $\mu\text{m}$  active area while maintaining a reset time of only 5 ns. We demonstrate nanoscale antenna-like structures to achieve exceptional efficiency and speed in single-photon detection.

© 2010 Optical Society of America

**OCIS codes:** (030.5260) Photon counting; (040.3060) Infrared; (040.5160) Photodetectors; (040.5570) Quantum detectors; (270.5570) Quantum detectors; (220.4241) Nanostructure fabrication; (050.6624) Subwavelength structures.

---

## References and links

1. H. Takesue, S. W. Nam, Q. Zhang, R. Hadfield, T. Honjo, K. Tamaki, and Y. Yamamoto, "Quantum key distribution over a 40-dB channel loss using superconducting single-photon detectors," *Nature Photon.* **1**, 343-348 (2007).
2. Q. Zhang, H. Takesue, S. W. Nam, C. Langrock, X. Xie, B. Baek, M. M. Fejer, and Y. Yamamoto, "Distribution of time-energy entanglement over 100 km fiber using superconducting single-photon detectors," *Opt. Express* **16**, 5776-5781 (2008).
3. T. Honjo, S. W. Nam, H. Takesue, Q. Zhang, H. Kamada, Y. Nishida, O. Tadanaga, M. Asobe, B. Baek, R. Hadfield, S. Miki, M. Fujiwara, M. Sasaki, Z. Wang, K. Inoue, and Y. Yamamoto, "Long-distance entanglement-based quantum key distribution over optical fiber," *Opt. Express* **16**, 19118-19126 (2008).
4. B. S. Robinson, A. J. Kerman, E. A. Dauler, R. O. Barron, D. O. Caplan, M. L. Stevens, J. J. Carney, S. A. Hamilton, J. K. W. Yang, and K. K. Berggren, "781 Mbit/s photon-counting optical communications using a superconducting nanowire detector," *Opt. Lett.* **31**, 444-446 (2006).
5. T. Zhong, X. Hu, F. N. C. Wong, K. K. Berggren, T. D. Roberts, and P. Battle, "High-quality fiber-optic polarization entanglement distribution at 1.3  $\mu\text{m}$  telecom wavelength," *Opt. Lett.* **35**, 1392-1394 (2010).

6. E. A. Dauler, M. J. Stevens, B. Baek, R. J. Molnar, S. A. Hamilton, R. P. Mirin, S. W. Nam, and K. K. Berggren, "Measuring intensity correlations with a two-element superconducting nanowire single-photon detector," *Phys. Rev. A* **78**, 053826 (2008).
7. G. N. Gol'tsman, O. Okunev, G. Chulkova, A. Lipatov, A. Semenov, K. Smirnov, B. Voronov, A. Dzardanov, C. Williams, and R. Sobolewski, "Picosecond superconducting single-photon optical detector," *Appl. Phys. Lett.* **79**, 705–707 (2001).
8. K. M. Rosfjord, J. K. W. Yang, E. A. Dauler, A. J. Kerman, V. Anant, B. Voronov, G. N. Gol'tsman, and K. K. Berggren, "Nanowire single-photon detector with an integrated optical cavity and anti-reflection coating," *Opt. Express* **14**, 527–534 (2006).
9. X. Hu, T. Zhong, J. E. White, E. A. Dauler, F. Najafi, C. Herder, F. N. C. Wong, and K. K. Berggren, "Fiber-coupled nanowire photon counter at 1550 nm with 24% system detection efficiency," *Opt. Lett.* **34**, 3607–3609 (2009).
10. A. Divochiy, F. Marsili, D. Bitauld, A. Gaggero, R. Leoni, F. Mattioli, A. Korneev, V. Seleznev, N. Kaurova, O. Minaeva, G. Gol'tsman, K. Lagoudakis, G. Konstantinos, M. Benkhaoul, F. Levy, and A. Fiore, "Superconducting nanowire photon-number-resolving detector at telecommunication wavelengths," *Nature Photon.* **2**, 302–306 (2008).
11. S. Miki, M. Takeda, M. Fujiwara, M. Sasaki, and Z. Wang, "Compactly packaged superconducting nanowire single-photon detector with an optical cavity for multichannel system," *Opt. Express* **17**, 23557–23564 (2009).
12. R. W. Heeres, S. N. Dorenbos, B. Koene, G. S. Solomon, L. P. Kouwenhoven, and V. Zwiller, "On-chip single plasmon detection," *Nano Lett.* **10**, 661–664 (2010).
13. A. J. Kerman, E. A. Dauler, W. E. Keicher, J. K. W. Yang, K. K. Berggren, G. Gol'tsman, and B. Voronov, "Kinetic-inductance-limited reset time of superconducting nanowire photon counters," *Appl. Phys. Lett.* **88**, 111116 (2006).
14. X. Hu, C. W. Holzwarth, D. Masciarelli, E. A. Dauler, and K. K. Berggren, "Efficiently coupling light to superconducting nanowire single-photon detectors," *IEEE Trans. Appl. Supercond.* **19**, 336–340 (2009).
15. T. W. Ebbesen, H. J. Lezec, H. F. Ghaemi, T. Thio, and P. A. Wolff, "Extraordinary optical transmission through sub-wavelength hole arrays," *Nature (London)* **391**, 867–869 (1998).
16. R. Mühlischlegel, H. -J. Eisler, O. J. F. Martin, B. Hecht, D. W. Pohl, "Resonance optical antennas," *Science* **308**, 1067–1069 (2005).
17. C. Genet, and T. W. Ebbesen, "Light in tiny holes," *Nature (London)* **445**, 39–46 (2007).
18. E. Cubukcu, E. A. Kort, K. B. Crozier, and F. Capasso, "A Plasmonic laser antenna," *Appl. Phys. Lett.* **89**, 093120 (2006).
19. L. Tang, S. E. Kocabas, S. Latif, A. K. Okyay, D. -S. Ly-Gagnon, K. C. Saraswat, and D. A. B. Miller, "Nanometre-scale germanium photodetector enhanced by a near-infrared dipole antenna," *Nature Photon.* **2**, 226–229 (2008).
20. A. V. Akimov, A. Mukherjee, C. L. Yu, D. E. Chang, A. S. Zibrov, P. R. Hemmer, H. Park, and M. D. Lukin, "Generation of single optical plasmons in metallic nanowires coupled to quantum dots," *Nature (London)* **450**, 402–406 (2007).
21. X. Hu, E. A. Dauler, A. J. Kerman, J. K. W. Yang, J. E. White, C. H. Herder, and K. K. Berggren, "Using surface plasmons to enhance the speed and efficiency of superconducting nanowire single-photon detectors," 2009 Conference on Lasers and Electro-Optics and Quantum Electronics and Laser Science Conference, 2347–2348 (2009).
22. F. J. García-Vidal, and L. Martín-Moreno, "Transmission resonances on metallic gratings with very narrow slits," *Phys. Rev. Lett.* **83**, 2845–2848 (1999).
23. F. J. García-Vidal, and L. Martín-Moreno, "Transmission and focusing of light in one-dimensional periodically nanostructured metals," *Phys. Rev. B* **66**, 155412 (2002).
24. J. Bravo-Abad, L. Martín-Moreno, and F. J. García-Vidal, "Transmission properties of a single metallic slit: From the subwavelength regime to the geometrical-optics limit," *Phys. Rev. E* **69**, 026601 (2004).
25. G. Veronis, and S. Fan, "Theoretical investigation of compact couplers between dielectric slab waveguides and two-dimensional metal-dielectric-metal plasmonic waveguides," *Opt. Express* **15**, 1211–1221 (2007).
26. B. A. Munk, *Frequency Selective Surface: Theory and Design* (Wiley, 2000).
27. E. D. Palik, *Handbook of Optical Constants of Solids* (Academic Press, Inc. 1998).
28. V. Anant, A. J. Kerman, E. A. Dauler, J. K. W. Yang, K. M. Rosfjord, and K. K. Berggren, "Optical properties of superconducting nanowire single-photon detectors," *Opt. Express* **16**, 10750–10761 (2008).
29. E. A. Dauler, B. S. Robinson, A. J. Kerman, J. K. W. Yang, K. M. Rosfjord, V. Anant, B. Voronov, G. Gol'tsman, and K. K. Berggren, "Multi-element superconducting nanowire single-photon detector," *IEEE Trans. Appl. Supercond.* **17**, 279–284 (2007).
30. X. Hu, F. Marsili, F. Najafi, and K. K. Berggren, "Mid-infrared single-photon detection using superconducting nanowires integrated with nano-antennae," 2010 Quantum Electronics and Laser Science Conference, QThD5 (2010).

## 1. Introduction

Applications, such as long-distance quantum key distribution (QKD) [1, 2, 3], photon-counting classical optical communication [4], infrared photonic entanglement distribution [5], and characterization of the photon statistics of light sources [6], require efficient and fast photon counters that operate at infrared wavelengths. In particular, these devices are critical enabling components in integrated quantum-information-processing systems. Superconducting nanowire single-photon detectors (SNSPDs) [7, 8, 9, 10, 11] are an emerging technology for efficient and fast infrared photon counting whose potential has been demonstrated in several experiments [1, 2, 3, 4, 5, 6]. Recently, integration of plasmonic structures with these devices has demonstrated single-surface-plasmon detection using SNSPDs [12]. However, all these devices suffer from a fundamental trade-off between the need to maximize their detection efficiency and the need to minimize their reset time [13, 14].

The device operating speed is limited by the details of the electrical mechanism of photodetection. The nanowire is typically made of niobium nitride (NbN) on a sapphire [7, 8, 9] or magnesium oxide (MgO) substrate [10, 11]. Once a single incident photon is absorbed by the NbN nanowire with a bias current slightly below the critical current of the superconducting nanowire, a resistive region is generated [7], resulting in diversion of the bias current into an amplifier, and a detectable voltage pulse. The absorbed energy eventually dissipates into the substrate, and the bias current recovers. The recovery time of the current, which limits the maximum detection rate, is determined by the kinetic inductance of the nanowire [13]. Because the kinetic inductance is proportional to the length of the nanowire, short nanowires are faster.

In direct conflict with the need for a short nanowire to optimize speed, a long nanowire is generally required to optimize detection efficiency. The  $\sim 4$ -nm-thick nanowire is as narrow as 70 to 100 nm, one order of magnitude narrower than the diffraction limit of the incident infrared radiation, resulting in a small overlap between the optical field and the nanowire. This small overlap limits the optical absorption, and thus also the efficiency of the nanowire. Practical applications require long, and thus highly inductive nanowires to be tightly wound into a  $\sim 200$ -nm-pitch meander [8, 9] to increase this spatial overlap and enhance the absorption. Hence, in conventional device design, efficiency must be sacrificed for speed, or vice versa.

In recent years, there has been tremendous interest in nano-metallic structures [15, 16, 17] and using these nanostructures to enhance the performance of active optoelectronic components. In particular, researchers have integrated a bow-tie antenna on the facet of a laser diode to intensify the light at the nanoscale [18]. In addition, researchers have integrated a germanium photodiode with a dipole antenna to enhance the photocurrent [19]. In quantum optics, researchers have used silver nanowires to enhance the non-classical light emission from single quantum dots [20].

Here, we integrate an SNSPD with optical nano-antennae to enhance its performance at detecting single photons from the far field. We have proposed a photonic structure that can increase the nanowire optical absorptance without having to increase its length, thus achieving good efficiency while preserving detector speed [14, 21]. In this paper, we demonstrate this device experimentally. We elaborate the concept of nano-antennae integration and the mechanism of absorption enhancement, explain the fabrication process in detail, present the characterization of the fabricated devices, and compare the performance of the antenna-integrated SNSPDs with the performance of previously reported devices.

## 2. Concept and mechanism

In order to make the detector simultaneously fast and efficient, we need to use a short nanowire that can absorb incident photons effectively, assisted by additional photonic structures. Suppose that we want to cover a practical active area, for instance,  $9\ \mu\text{m}$  by  $9\ \mu\text{m}$ , with a NbN nanowire

meander. We can either use a dense meander as shown in Fig. 1 (a) or use a sparse meander as shown in Fig. 1 (b). The length of the nanowire in the dense meander with a small pitch is longer, and, therefore, the detector is slow because of the large kinetic inductance. In contrast, the length of the nanowire in the sparse meander with a large pitch is shorter, and, therefore, the detector is fast because of the small kinetic inductance. However, the nanowire in a large pitch meander cannot absorb incident photons efficiently because most of the incident photons simply pass through the gaps.

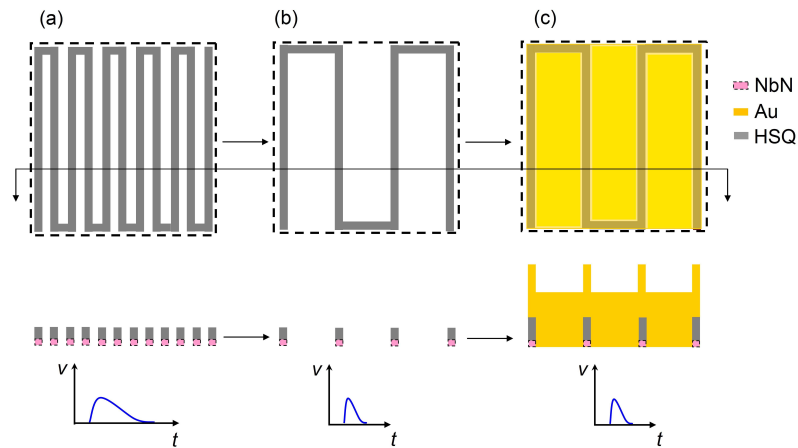


Fig. 1. Explanation of the concept development of the superconducting nanowire single-photon detector integrated with optical nano-antennae. The upper panel shows the plan-view schematics of the device structures. The middle panel shows the cross sections. The lower panel shows schematics of the output signals. In order to cover an area with NbN nanowire meander, a dense meander in (a) or a sparse meander in (b) can be used. The nanowire in (a) is long, so that the detector is slow; the nanowire in (b) is short, so that the detector is fast. However, the large gaps between adjacent nanowires in (b) allow incident photons to pass through the gaps, so that the absorption is weak. As shown in (c), the idea is to both fabricate the HSQ structure with appropriate height and put gold between the adjacent HSQ structures and on top of the HSQ to collect the incident photons, block the path of transmission, and reduce reflection.

A schematic of the device structure with nano-antennae integration is shown in Fig. 1 (c). The differences between this design and the design of SNSPDs realized in the past [8, 9] are that here, a sparser meander with a pitch larger than 200 nm is used, and hydrogen silsesquioxane (HSQ) fence-like structures on top of the nanowire and the surrounding gold form the optical nano-antennae, which can efficiently collect and localize the incident photons in the NbN material, eliminating optical transmission and reducing reflection.

The operating principle of the optical nano-antennae is primarily based on two physical effects: (1) non-resonant nano-optical collection by a metallic slit and (2) resonant enhancement of absorption by an optical nano-cavity backing the slit. A third effect resulting in a smaller additional enhancement due to resonant scattering of fields along the gold-sapphire interface also plays a role. These nano-optical mechanisms act collectively to increase the field density in the nanowire and the effective absorption cross-section of the NbN structure for incident light with transverse-magnetic (TM) polarization. A quantitative way to understand these effects is to solve Maxwell's Equations by performing optical simulation on the whole structure; however, to provide some physical insight into the influence of each effect in isolation, we start from a

simple model with only one slot, then add cavities, and expand to consider multiple slots.

The first effect, the non-resonant nano-optical collection effect, is based on the fact that the effective collection area of a subwavelength slit for TM-polarized light is larger than the geometric area of the slit. In other words, the subwavelength slit can collect and focus the incident light into the nano-slit [22, 23, 24, 25], acting like a feed gap. Here, we use this effect to collect the light and focus onto NbN, and enhance the absorption of NbN. We simulated a similar one-dimensional gold-HSQ-gold slot with NbN at its aperture as shown in the inset of Fig. 2, in which  $k$  represents the wavevector,  $E$  the electric field, and  $w$  the width of the slot. In this paper, we only consider the perpendicular illumination by a plane wave, i.e., the wavevector,  $k$ , of the incident light is in the  $z$ -direction. For TM polarization, as shown in the inset of Fig. 2, the electric field is polarized in the  $x$ -direction and the magnetic field is polarized in the  $y$ -direction; for transverse-electric (TE) polarization, the electric field is polarized in the  $y$ -direction and the magnetic field is polarized in the  $x$ -direction. The wavelength used in the simulation and experiment in this paper is 1550 nm. We found that the gold structure as shown in the inset of Fig. 2 enhances the absorption of the NbN nanowire. To quantify this enhancement, we define absorption enhancement as the ratio of absorption per unit width in the nanowire normalized to the absorption of an unpatterned NbN film per unit width. Intuitively speaking, this defined parameter describes the capability of added photonic structures to enhance the absorbed energy density inside NbN. Fig. 2 presents this absorption enhancement. The absorption enhancement of an 80-nm-wide (the value of the nanowire width in our experiment) NbN nanowire is approximately 2, and approaches 1 for an infinitely wide slot. The absorption enhancement decreases monotonically, except for a few fine features, with the increase of the slot width. Currently, it is not certain what the fine features are due to, however their reproducibility and independence of simulation parameters suggests that they are real, and not simply a numerical effect. But this almost monotonic decrease, together with the strongly enhanced electric field observed in the simulation at the gold edge adjacent to the NbN, suggests the existence of non-resonant edge-scattering effect in this system.

In the second effect, the resonant enhancement of absorption by an optical nano-cavity backing the slit, the effective interaction time between the photon and the nanowire is increased due to cavity resonance. As shown in the inset of Fig. 3, each gold-HSQ-gold slot behaves as a resonant optical waveguide, while a reflector behind the waveguide forms a cavity, eliminating optical transmission and reducing reflection. The photons are thus strongly absorbed by the nanowire placed at the waveguide aperture, where the electric field is maximal, i.e., at the field anti-node created by the resonator. By performing optical simulation on a single cavity, we optimized the cavity length,  $l$ , defined as the vertical distance from the top of the HSQ to the sapphire-NbN interface. Fig. 3 presents the absorption enhancement of the NbN nanowire as a function of  $l$ . The width of the nanowire was fixed at 80 nm. The absorption enhancement oscillates with the cavity length, demonstrating the cavity effect. The first absorptance-enhancement peak appears at 150-nm cavity length and decreases at either shorter or longer cavity lengths around 150 nm. At this optimum cavity length, the absorption enhancement is increased by the cavity from  $\sim 2$  to  $\sim 6$ . The slow decrease in absorptance for cavity length either shorter or longer than the optimum permits a wide tolerance of cavity-length inaccuracy in fabrication.

We used a one-dimensional, periodic structure as shown in Fig. 4 (a) to simulate the nanowire meander with gold optical nano-antennae. Fig. 4 (b) presents the simulated absorption enhancement and absolute absorptance, defined as the absorbed optical power normalized to incident optical power, as a function of pitch,  $p$ , fixing  $w$  and  $l$  to be the experimental values 80 nm and 180 nm, respectively. This calculation includes the non-resonant nano-optical collection and resonant cavity effects as well as a third effect that we attribute to resonant scattering of the field at the gold-sapphire interface. At small pitches, the absorption enhancement is suppressed

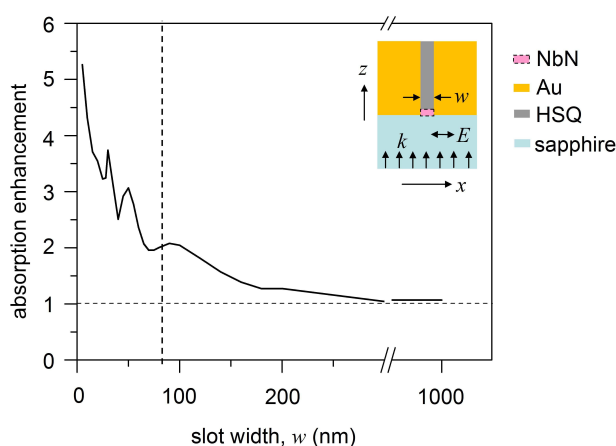


Fig. 2. Study of the non-resonant nano-optical collection effect. The figure shows the absorption enhancement as a function of the width of the slot,  $w$ . The model studied is shown in the inset. The model consists of a gold-HSQ-gold slot waveguide on top of a sapphire substrate and the NbN nanowire at the aperture of the waveguide. The experimental value of the width of the nanowire is 80 nm. The monotonic decrease, except for a few fine features, of the absorption enhancement with the increase of the slot width suggests that this effect is an edge effect.

because the antenna aperture of each unit cell overlaps that of adjacent cells. By increasing the pitch, more light is concentrated into each slot and absorbed by the NbN nanowire. The absorption enhancement factor would saturate at a very large pitch if each individual antenna did not interfere with the others. However, when the pitch of the NbN nanowire is equal to integer numbers of  $\lambda/n$ , where  $n$  is the optical index of sapphire, most of the incident light is reflected by the gold instead of being coupled to the optical nano-cavities and NbN nanowire; therefore, the absorption of the NbN is minimized. The interface between sapphire and nano-structured gold thus behaves as a frequency selective surface [26]. The initial increase of absorption enhancement with the pitch and the minimum at  $p = 886$  nm result in a peak of absorption enhancement at the pitch of  $\sim 600$  nm, which was therefore chosen for our experiment. Correspondingly, the maximum absorption enhancement is 8,  $\sim 25\%$  of which is due to this frequency-selective-surface effect. In addition, Fig. 4 (b) presents the absolute absorptance as a function of  $p$ . For a 600-nm pitch, the absolute absorptance is calculated to be 47% for TM-polarized light.

We note that the mechanism of the enhancement presented here is not quite related to surface plasmon *resonance* although the device structure contains cavities composed of surface-plasmon-polariton slots, operating at the wavelength of 1550 nm, and reflectors. We verified this by replacing the gold with a perfect electric conductor (which would not support surface plasmon resonances), and observed that similar absorption enhancement was still obtained.

The optical simulations in this section were done by using commercial software Comsol Multiphysics based on the finite-element method. The optical indices for NbN [14], NbNO<sub>x</sub> [14], gold [27], HSQ [14], and sapphire [14] that we used in simulations were  $5.23 + 5.82j$ , 2.28,  $0.55 + 11.5j$ , 1.39, and 1.75, respectively, where  $j = \sqrt{-1}$ . The thickness of the NbN is 4.5 nm. The exterior boundary conditions for the horizontal boundaries we used were always scattering



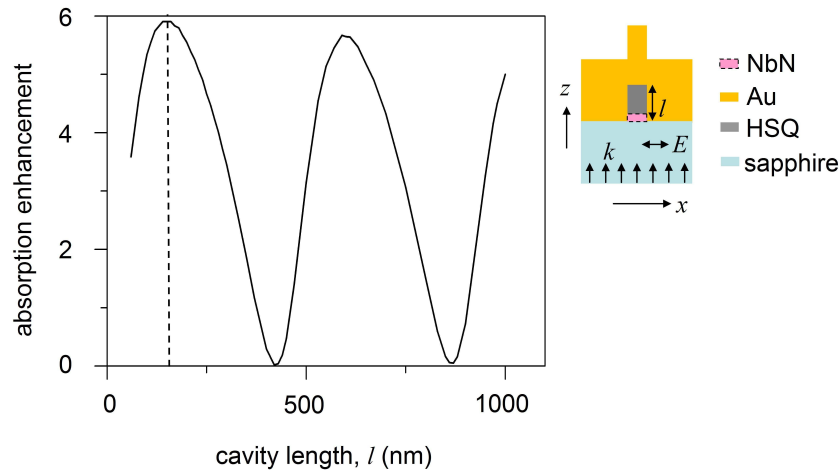


Fig. 3. Study of the resonant nano-optical cavity effect. This figure shows the simulated absorption enhancement as a function of cavity length,  $l$ . The model studied is shown in the inset. The absorption enhancement peaks at  $l \sim 150$  nm and, correspondingly, the absorption enhancement, including the nonresonant collection effect, reaches  $\sim 6$ .

boundary conditions. For the vertical boundaries, we used scattering boundary conditions when simulating a single slot, and used periodic boundary conditions when simulating the meander. When simulating a single slot, the width of the modeled region in the simulation was  $20 \mu\text{m}$ .

Figure 5 (a) presents the distribution of optical intensity, which is proportional to the square of the amplitude of the electric field, and the time-averaged Poynting vectors, assuming  $l = 180$  nm,  $w = 80$  nm, and  $p = 600$  nm. The collection effect of the optical nano-antennae is clearly seen. Figure 5 (b) shows the intensity distribution along the white dashed line in (a), illustrating that the NbN is positioned near the field maximum.

### 3. Device fabrication and imaging

We successfully fabricated the SNSPDs integrated with optical nano-antennae. Starting from a 4.5-nm thick NbN film on a sapphire substrate, we first fabricated gold contact pads. To do this, we spun on  $\sim 1 \mu\text{m}$  of Shipley Microposit S1813, a positive-tone photoresist, baked the chip in ambient conditions at  $90^\circ\text{C}$  for 3 min, performed contact optical lithography to define the pads, and developed the resist. After evaporating 10-nm titanium (Ti) and 50-nm gold (Au), we performed lift-off in  $90^\circ\text{C}$  1-methyl-2-pyrrolidinone (NMP) solvent. The Ti layer was used to enhance the adhesion between Au and NbN. We then spun on  $\sim 300$ -nm HSQ formulated as Fox-14 from Dow Corning, and performed scanning-electron-beam lithography at 30 kV to define the structure of the nanowire meander, followed by developing the HSQ in 25% tetramethylammonium hydroxide (TMAH) for 4 min at  $\sim 20^\circ\text{C}$ . We used reactive-ion etching (RIE) to transfer the pattern into NbN from HSQ with tetrafluoromethane ( $\text{CF}_4$ ) as the reactive gas and RF power of 98 W (power density:  $\sim 1.5 \text{ Wcm}^{-2}$ ) for 100 sec. The resulting thicknesses of HSQ measured by both atomic force microscopy and scanning-electron-beam cross-section imaging were  $180 \pm 10$  nm. To integrate the nanowire detector with the optical nano-antennae, we then spun on  $\sim 1 \mu\text{m}$  of S1813 a second time, performed contact optical lithography aligned with the detector to open a window of  $25 \mu\text{m}$  by  $25 \mu\text{m}$  for the structure of

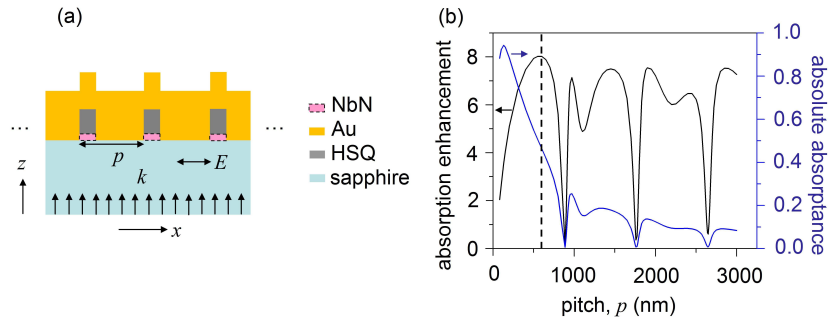


Fig. 4. Absorption enhancement by the optical nano-antennae. (a) shows the model used in this study. It is an infinite periodic structure with the unit cell shown in the inset of Fig. 3. The pitch of the structure is denoted as  $p$ . (b) shows the absorption enhancement (left y-axis) and absolute absorbance (right y-axis) as a function of the pitch,  $p$ . The inference pattern is due to the nanostructured interface between the gold and the sapphire substrate, which forms a frequency-selective surface. The interference makes the total absorption enhancement, including three effects, peak at the pitch 600 nm. The maximum absorption enhancement is  $\sim 8$ , and the corresponding absolute absorbance is 47%.

the gold antennae. After evaporating  $\sim 6$ -nm  $\text{SiO}_2$  for electrically insulating the nanowire from the Ti and Au, followed by  $\sim 3$ -nm Ti, and  $\sim 300$ -nm Au, we did lift-off in  $90^\circ\text{C}$  NMP.

A sample detector was cut by focused-ion beam and imaged by electron beam using a Zeiss NVision 40 dual beam system. We first deposited  $\sim 2$ - $\mu\text{m}$  thick platinum (Pt) *in-situ* in a  $2$ - $\mu\text{m}$ -by- $10$ - $\mu\text{m}$  area to protect the device structure from being damaged by the focused gallium ions. The cut was done sequentially by a coarse mill (30 kV, 700 pA), a medium mill (30 kV, 300 pA) and a final fine polish (30 kV, 40 pA). The cross-section was then imaged by electron beam at 2 kV using the secondary-electron detector. Although the chip was tilted so that the angle between the normal to the chip and the incident electron beam was  $54^\circ$ , the image was obtained after digital angle-correction.

Figure 6 presents the plan-view (a) and cross-section (b) scanning-electron micrographs of the detector. The SNSPD was composed of a  $135$ - $\mu\text{m}$  long NbN nanowire wound in a boustrophedonic pattern across an effective area of  $9$   $\mu\text{m}$  by  $9$   $\mu\text{m}$ . In Fig. 6 (a), the linear structures surrounding the active area are required for proximity-effect correction in scanning-electron-beam lithography. The HSQ fence-like structures on top of the NbN nanowire are  $\sim 80$ -nm wide and  $\sim 180$ -nm tall. The pitch of the meander is 600 nm. By comparing the fabricated structure in Fig. 6 (b) with the schematic in Fig. 1 (c), we find that they are slightly different. In Fig. 6 (b), the gold structures between adjacent HSQ fence-like structures are in the shape of a trapezoid, and voids exist between the gold and the HSQ fence-like structures. These voids resulted from migration of the gold on top of the HSQ during the evaporation process, which gradually shadowed the subsequent evaporation, as shown in Fig. 7 (a).

We evaluated the effect of the voids on the absorbance of the nanowire by simulating the structure obtained. From the cross-section micrograph in Fig. 6 (b), we drew in Fig. 7 (b) the geometry of a unit cell used in finite-element optical simulation. We found that the voids decreased the simulated absorbance from 47% to 44%.

To eliminate the voids, one could use a two-angle evaporation process to coat the sidewalls of HSQ with gold. If the evaporation angles are sufficiently small, and if a slightly re-entrant photoresist profile is used around the edge of the metal-deposited region to avoid sidewall coat-

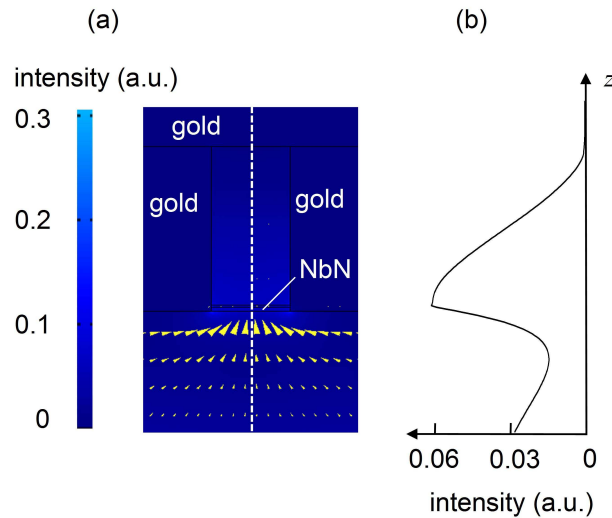


Fig. 5. Simulated intensity distribution and time-averaged Poynting vectors. In (a), the surface color represents the field intensity and the arrows show the time-average Poynting vectors. The capability of collecting and focusing the incident light by the optical nano-antennae can be seen. In (b), the line shows the intensity distribution along the white dashed line in (a), illustrating that the NbN nanowire is positioned near the field maximum.

ing of metal on the photoresist, two-angle evaporation may be compatible with the subsequent lift-off required.

#### 4. Device characterization

We characterized the fabricated SNSPDs integrated with optical nano-antennae by measuring the device efficiency, kinetic inductance, and timing jitter. From the measured kinetic inductance, we calculated the reset time.

##### 4.1. Device efficiency

Device efficiency is defined as the probability that a photon reaching the active area of the SNSPD results in a voltage pulse [8]. In our experiment, we used a greatly attenuated pulsed laser, with a pulse repetition rate of 10 MHz, to generate single photons at the wavelength of 1550 nm. Device efficiency was measured at a baseplate temperature of 2.1 K using a cryogenic probe station. We used a polarization controller in the optical illumination path to maximize or minimize the counting rate, and considered the polarization with the maximized counting rate as TM polarization and the minimized as TE polarization. In our measurement, we confirmed that the polarizations with the maximum and minimum counting rates for a detector integrated with nano-antennae corresponded to the polarizations with the minimum and maximum counting rates, respectively, for a detector without antenna-integration on another chip mounted adjacent to this chip with the same device orientation.

Device efficiency,  $\eta$ , for both polarizations as a function of normalized bias current,  $i_b/I_c$ , is presented in Fig. 8. Once the detector was biased at 97.5% of  $I_c$ , which was 11.7  $\mu\text{A}$  at the temperature of 2.1 K, device efficiency reached  $47 \pm 5\%$  for TM polarization and  $3.5 \pm 0.4\%$  for TE polarization. The fractional error in the detection efficiency measurement was estimated to

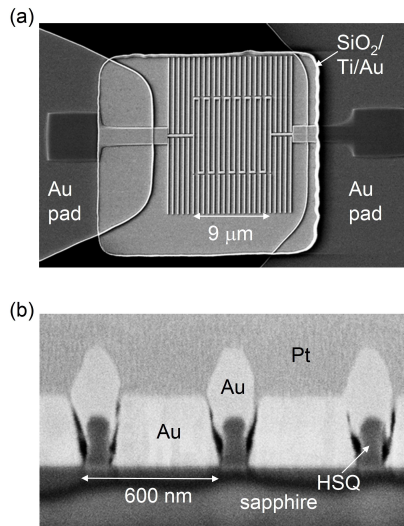


Fig. 6. Scanning-electron micrograph of the fabricated superconducting nanowire single-photon detector integrated with optical nano-antennae. (a) shows a plan-view scanning-electron micrograph. The active area of the detector is  $9\ \mu\text{m}$  by  $9\ \mu\text{m}$ . The linear structures surrounding the active area are required for proximity-effect correction in scanning-electron-beam lithography. (b) shows a cross-section image. The HSQ fence-like structures are  $\sim 80\text{-nm}$  wide and  $\sim 180\text{-nm}$  tall. The pitch of the meander is  $600\ \text{nm}$ . The NbN nanowire itself is under the HSQ and is not visible on the micrograph. The gold surrounding the HSQ fence-like structures forms the optical nano-antennae. Each gold structure between two adjacent HSQ fence-like structures was observed to be in the shape of a trapezoid, resulting in voids between the gold and the HSQ fence-like structures. These voids were attributed to migration of the gold on top of the HSQ fence-like structures during the evaporation process, which gradually shadowed the subsequent evaporation.

be  $\sim 10\%$ , primarily due to the calibration of the optical-spot diameter. For this device, we did not coat the back of the sapphire substrate with an anti-reflection coating (ARC) as done in prior work [8]; if we take the calculated  $7.4\%$  reflectance at the air-sapphire interface into account, the corrected device efficiencies for TM and TE polarizations were  $50 \pm 5\%$  and  $3.8 \pm 0.4\%$ , respectively. The response of the detector to TE-polarized incident light is suppressed because the optical nano-cavities do not support TE modes so that most of the incident TE-polarized light was reflected.

The  $47\%$  device efficiency for TM-polarized light would be surprising if one did not consider the effects described above, given that the fill-factor of NbN nanowire was only  $\sim 13\%$ . Furthermore, given that the intrinsic quantum efficiency,  $P_R$ , is estimated to be  $70\%$  to  $90\%$  [28], the majority of incident light was coupled into the NbN nanowire, i.e., the absorptance of the NbN nanowire must be  $> 50\%$  for TM polarization. As a comparison, the absorptance of the  $80\text{-nm}$  wide NbN nanowire in the  $600\text{-nm}$  pitch meander on the sapphire substrate without any optical nano-antenna integration was simulated to be  $4\%$  and  $8\%$  for TM and TE polarizations, respectively.

To further support the thesis that the optical nano-antenna plays an important role in device performance, we calculated polarization ratios, defined as device efficiency of TM polarization relative to TE polarization at the same bias current,  $97.5\%$  of  $I_c$ . The calculated ratio from the measured device efficiencies was  $\sim 13$  for this antenna-integrated device, as opposed to  $\sim 0.5$

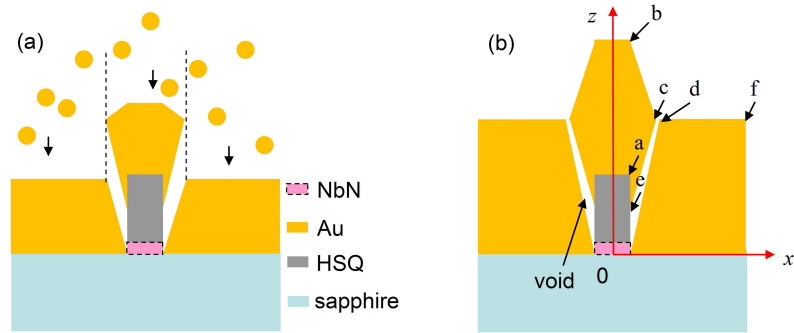


Fig. 7. Cross-section schematic illustrating the appearance of voids and the model used for evaluating the effect of the voids on the absorption of the NbN nanowire. (a) These voids were attributed to migration of the gold on top of the HSQ during the evaporation process, which gradually shadowed the subsequent evaporation. (b) The geometry of a unit cell was used in finite-element optical simulation. A coordinate system was established to define the geometry. The  $x$  and  $z$  coordinates in nm for the points a, b, c, d, e, and f were (40, 186.5), (40, 486.5), (110, 300), (120, 300), (40, 90), and (300, 300), respectively.

for a 600-nm-pitch detector without antenna-integration.

The presented results focused on a single device out of 45 devices fabricated. Fig. 9 presents maximum efficiency (TM polarization) and minimum efficiency (TE polarization) for the 4 of these 45 devices that showed maximum efficiency exceeding 10%. The ratio of device efficiency for TM and TE polarizations is a key signature of the antenna effect, and this effect was observed in all four of the devices.

Two challenges in the fabrication process limited the yield; understanding these challenges should permit further improvement in device yield and performance. The first challenge was direct electron-beam writing on thick HSQ resist. The resist used in this experiment was 300-nm thick, as opposed to the 70-nm thickness typically used [8]. Thicker resists scatter electrons over a greater area, and, therefore, the dose control required to yield uniform nanowires was more difficult for these devices. To reduce the scattering of electrons in thick HSQ in future work, one could, for example, increase the acceleration voltage from 30 kV to 100 kV. The second fabrication challenge was gold evaporation. During the cryogenic testing, we observed that some devices with similar critical currents differed significantly in device efficiency, suggesting that the absorptance was different among devices. This difference might be due to variation in the migration of gold during the evaporation process, which caused voids of varying shapes. To address this challenge, one could use a re-entrant photoresist profile and two-angle evaporation.

#### 4.2. Kinetic inductance and reset time

After a detection event, the SNSPD cannot immediately detect another incident photon because the bias current cannot flow back to the nanowire and, therefore, the device efficiency (in fact, due to  $P_R$ ) cannot recover immediately. The reset time,  $\tau$ , is defined as the time needed for the device efficiency, after a detection event, to recover to 90% of the device efficiency if there were no detection. The recovery of the bias current, and, therefore, the detection efficiency, is known to be limited by the kinetic inductance [13],  $L_k$ .

We measured the kinetic inductance of the detector to be 100 nH using a network analyzer, and then calculated the reset time. The calculation is composed of two steps. First, from the measured  $\eta - i_b$  relation, we can obtain the bias current  $I_{90\%}$  at which the device efficiency is

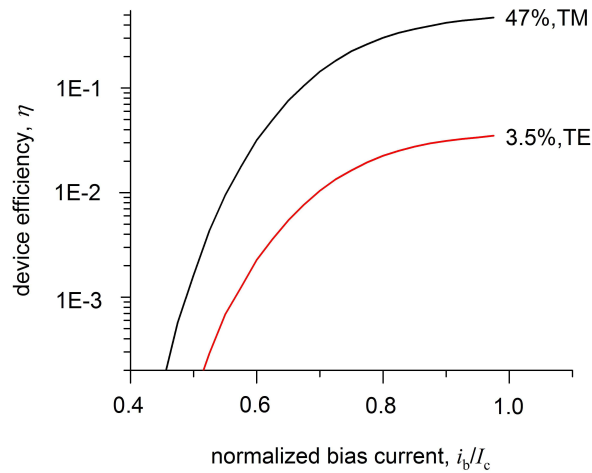


Fig. 8. Graph of measured device efficiency for both TM and TE polarizations as a function of normalized bias current,  $i_b/I_c$ , where  $I_c$  is the critical current of the superconducting nanowire. The device efficiency was measured in a probe station at baseplate temperature of 2.1 K. When biased at 97.5% of its critical current, the device efficiency was 47% and 3.5% for TM and TE polarizations, respectively. The critical current,  $I_c$ , was 11.7  $\mu$ A.

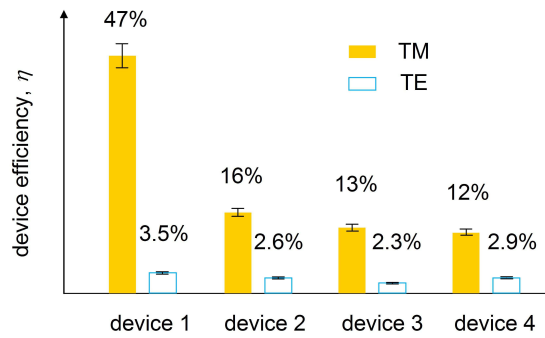


Fig. 9. Device efficiency of the detectors with maximum device efficiency larger than 10% on the chip. The dominant response to photons in the TM-polarized incident photons is the key feature of the antenna effect. Each error bar represents 10% fractional error, which is primarily due to the calibration of the optical-spot diameter in the device efficiency measurement.

90% of the device efficiency at  $I_b$ , which is the the bias current we set to operate the detector, by

$$I_{90\%} = \eta^{-1}[90\%\eta(I_b)], \quad (1)$$

where  $\eta^{-1}(\cdot)$  is the inverse function of  $\eta(\cdot)$ . Second, from  $L_k$ , we can obtain the reset time,  $\tau$ , which is the time needed for the current to recover from 0 to  $I_{90\%}$ , by

$$1 - \exp[-\tau/(L_k/R)] = I_{90\%}/I_b, \quad (2)$$

where  $R = 50 \Omega$ . Or equivalently,

$$\tau = (L_k/R)\ln[1/(1 - I_{90\%}/I_b)]. \quad (3)$$

In our experiment, the bias current was set to be  $I_b = 0.975I_c$ . We obtained  $I_{90\%} = 0.9I_c$  from  $\eta - i_b$  relation we measured (Fig. 8). We then calculated the reset time to be 5 ns.

#### 4.3. Timing jitter

Because the origin of timing jitter of the SNSPDs is not well understood, and because precise timing jitter is one of the advantages of this technology, one concern we had was whether adding the optical nano-antennae to the superconducting nanowire would significantly affect the timing jitter of the detector. To address this concern, we measured timing jitter for TM and TE polarizations to be  $39 \pm 3$  ps and  $45 \pm 3$  ps, respectively, biasing the detector at 97.5% of its  $I_c$ .

We measured the timing jitter of the SNSPD integrated with optical nano-antennae using the same method and experimental setup used in [29]. The output pulses from a passively mode-locked fiber laser, with a pulse repetition rate of 10 MHz and a pulse width of less than 1 ps, were split into two channels by an optical splitter, and were sent to the SNSPD and a reference photodiode with 40 GHz bandwidth. Their outputs were sent to two channels of a 6 GHz real-time oscilloscope. The front edge of the output of the SNSPD was used as the trigger, and the timing of the output of the photodiode was measured.

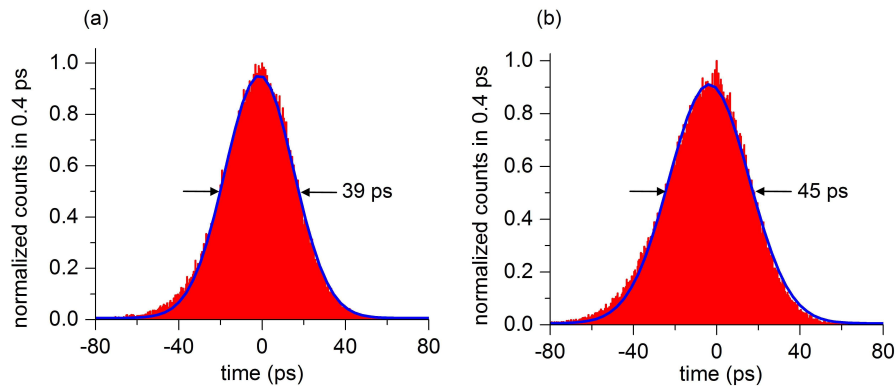


Fig. 10. Histogram of timing jitter of the superconducting nanowire single-photon detector integrated optical nano-antennae for (a) TM and (b) TE polarizations at the bias of 97.5% of the critical current of the nanowire. The lines are Gaussian fits, with full widths at half maxima of 39 ps and 45 ps for (a) TM and (b) TE polarizations, respectively.

The measured timing-jitter histograms and Gaussian fits are presented in Fig. 10 (a) for TM polarization and (b) for TE polarization. The Gaussian function used for fitting is expressed as

$$g(t) = g_0 + \frac{a}{\sigma\sqrt{\pi/2}} \exp\left[-\frac{2(t-t_0)^2}{\sigma^2}\right], \quad (4)$$

where  $g_0$ ,  $a$ , and  $\sigma$  are fitting parameters. The full width at half maximum equals  $1.18\sigma$ ; it is 39 ps for (a) TM polarization and 45 ps for (b) TE polarization. There was  $\pm 3$  ps uncertainty on each measured value because of the  $\pm 2$  ps uncertainty of trigger and interpolator jitter

specified by the oscilloscope. The difference between the measured values of the timing jitter for two polarizations may represent a measurement uncertainty, or a real difference between the timing jitter for different polarizations. Further investigations of the timing jitter would be required to resolve this issue.

## 5. Comparison with previously reported devices

In order to comprehensively compare the device efficiency, speed, and active area of this detector with previously reported devices, we define a figure of merit as  $A\eta/\tau$ , where  $A$  is device area,  $\eta$  is device efficiency, and  $\tau$  is reset time. Device efficiency of this detector was  $47 \pm 5\%$ , with reset time of  $\sim 5$  ns and active area of  $9 \mu\text{m} \times 9 \mu\text{m}$ . The figure of merit of this detector is thus  $\sim 7.6 \mu\text{m}^2/\text{ns}$ . As a comparison, the best previously published device efficiency for an SNSPD on sapphire [8] was  $57 \pm 6\%$ , with reset time of  $\sim 3.4$  ns and active area of  $3 \mu\text{m} \times 3.3 \mu\text{m}$ . Its figure of merit is calculated to be  $\sim 1.7 \mu\text{m}^2/\text{ns}$ . Thus, the figure of merit has been enhanced by a factor of 4.5. The large active area of this antenna-integrated SNSPD makes the coupling of light into the detector from fibers, waveguides, or free space much more efficient and convenient.

## 6. Conclusion

The key result of this paper is the integration of optical nano-antennae with an SNSPD to enhance the efficiency and speed of photodetection at the quantum level. The figure of merit has been enhanced by a factor of 4.5 compared with that of the SNSPD with the best device efficiency published in 2006 [8]. The active area, device efficiency, and reset time of this SNSPD are  $9 \mu\text{m}$  by  $9 \mu\text{m}$ , 47%, and 5 ns, respectively. This type of SNSPDs is the only type that dominantly responds to the TM-polarized incident photons.

This simultaneous enhancement of efficiency and speed is important in many applications where efficiency and speed of infrared single-photon detection are essential, including long-distance quantum key distribution (QKD) [1, 2, 3], photon-counting classical optical communication [4], infrared photonic entanglement distribution [5], and characterization of photon statistics of light sources [6].

This paper has focused on single-element SNSPDs, composed of 80-nm wide nanowires, integrated with optical nano-antennae. However, the concept and device structure developed here are quite general. For example, one could integrate a four-element SNSPD with optical nano-antennae to enhance the speed and efficiency, and further expand the active area of the device; one could also integrate ultra-narrow nanowires (width  $\leq 30$  nm) with optical nano-antennae to enhance the speed and efficiency to detect mid-IR single photons [30]. In this paper, we have demonstrated that optical nano-antennae can enhance optical collection in the single-photon regime. This capability to manipulate single photons in the near field of metal nanostructures may also be useful for other classical and quantum nano-optical devices, and similarly boost their performance.

## Acknowledgments

We acknowledge the technical help from N. Antoniou, J. M. Daley, M. K. Mondol, F. Najafi, and helpful discussion with Prof. M. Brongersma, Dr. F. Marsili, Prof. D. Staelin, Dr. B. -I. Wu, and Prof. E. Yablanovitch. Patterning of the detector was done in MIT's shared scanning-electron-beam-lithography facility. The experimental work at MIT campus was sponsored by IARPA and the National Science Foundation under NSF award no. ECCS-0823778. Modelling work was supported as part of the Centre for Excitonics, an Energy Frontier Research Center funded by the U.S. Department of Energy, Office of Science, Office of Basic Energy Sciences



under Award Number DE-SC0001088. At MIT Lincoln Laboratory, this work was sponsored by the United States Air Force under Air Force Contract #FA8721-05-C-0002. Opinions, interpretations, recommendations and conclusions are those of the authors and are not necessarily endorsed by the United States Government. The cross-section imaging of the detector in this work was done at the Centre for Nanoscale Systems (CNS), a member of the National Nanotechnology Infrastructure Network (NNIN), which is supported by the National Science Foundation under NSF award no. ECS-0335765. CNS is part of the Faculty of Arts and Sciences at Harvard University.